

# Superconducting vortex-charge measurement using cavity electromechanics

Sudhir Kumar Sahu,<sup>1</sup> Supriya Mandal,<sup>2</sup> Sanat Ghosh,<sup>2</sup> Mandar M. Deshmukh,<sup>2</sup> and Vibhor Singh<sup>1,\*</sup>

<sup>1</sup>*Department of Physics, Indian Institute of Science, Bangalore-560012 (India)*

<sup>2</sup>*Department of condensed matter physics and material sciences,  
Tata Institute of Fundamental Research, Mumbai - 400005 (India)*

As the magnetic field penetrates the surface of a superconductor, it results in the formation of flux-vortices. It has been predicted that the flux-vortices will have a charged vortex core and create a dipolelike electric field. Such a charge trapping in vortices is particularly enhanced in high- $T_c$  superconductors (HTS). Here, we integrate a mechanical resonator made of a thin flake of HTS  $\text{Bi}_2\text{Sr}_2\text{CaCu}_2\text{O}_{8+\delta}$  into a microwave circuit to realize a cavity-electromechanical device. Due to the exquisite sensitivity of cavity-based devices to the external forces, we directly detect the charges in the flux-vortices by measuring the electromechanical response of the mechanical resonator. Our measurements reveal the strength of surface electric dipole moment due to a single vortex core to be approximately  $30 |e|a_B$ , equivalent to a vortex charge per  $\text{CuO}_2$  layer of  $3.7 \times 10^{-2} |e|$ , where  $a_B$  is the Bohr radius and  $e$  is the electronic charge.

The penetration of a magnetic field in type-II superconductors in the form of Abrikosov vortices is well-known [1, 2]. Such vortices have a normal-core of size of the coherence length and each vortex is surrounded by a circulating supercurrent that decays over a characteristic magnetic length scale. It has been predicted that such vortices can trap charges [3–6]. The origin of the vortex charge can be understood from the difference in the chemical potentials in the superconducting-state and the normal region due to the particle-hole asymmetry. It leads to a redistribution of electrons to maintain the same electrochemical potential across a vortex [7], as shown schematically in Fig. 1(a). Intuitively, the idea of charged vortex core can also be captured by considering the inertial and Lorentz forces acting on the Cooper pairs encircling the normal core, resulting in the depletion of charges from the core [6].

To probe the trapped charge in the vortex core, the high- $T_c$  superconductors (HTS) are particularly attractive. The magnitude of the vortex charge is approximately given by  $|e|(\Delta/\epsilon_F)^2$ , where  $\Delta$  is the superconducting gap and  $\epsilon_F$  is the Fermi energy. The ratio  $\Delta/\epsilon_F$  is usually high in HTS ( $\Delta/\epsilon_F \sim 0.1$ ). Indeed, in the past, the inference of the charged vortex core has been made on bulk crystals of cuprate superconductors based on techniques probing the sign reversal of Hall coefficient [8], the nuclear quadrupole resonance [9, 10], and instability of the vortex lattice [11]. However, a measurement of the charged vortex core directly measuring its electrostatic field is a challenging task due to its small magnitude and screening by the surrounding charges.

In recent years, nanoelectromechanical systems based approach to probe phase transitions and the thermodynamical properties such as heat capacity, thermal conductivity, and magnetization have drawn a lot of attention [12–16]. Particularly, the integration of exfoliated thin flakes into cavity optomechanical and hybrid devices have resulted into enhanced sensitivity to external forces [17–19]. With these motivations in mind, we apply cavity

optomechanical techniques to detect the charges associated with vortices in a high- $T_c$  superconductor by directly probing their electrostatic effect.

In this work, we use a mechanical resonator of 5 unit cell (UC) thick exfoliated flake of  $\text{Bi}_2\text{Sr}_2\text{CaCu}_2\text{O}_{8+\delta}$  (BSCCO) and integrate it with a microwave cavity to realize a cavity electromechanical device. Due to their low mass, such mechanical resonators have a large coupling with the microwave field of the cavity, which enhances their force sensitivity. Fig. 1(b) shows the electrical equivalent schematic of the device. Such a device is analogous to a Fabry-Perot cavity with a mechanically compliant mirror, where vibrations of the mirror parametrically modulate the resonant frequency of the cavity [20]. We use a superconducting coplanar waveguide-based  $\lambda/4$  microwave cavity as shown in Fig. 1(c). The cavity is fabricated by patterning a 200 nm thick sputtered molybdenum and rhenium (MoRe) alloy film on top of intrinsic silicon wafer [21, 22]. The MoRe film has a  $T_c$  of 11 K. Near the coupler end of the microwave cavity, a feedline is selectively etched to reduce the MoRe film thickness by 120 nm. The difference in MoRe film thickness provides the clearance to form a suspended mechanical drumhead resonator by the transfer of an exfoliated BSCCO flake. A scanning electron microscopy (SEM) image of the suspended BSCCO flake after the transfer is shown in Fig. 1(d). In this configuration, the BSCCO drumhead-shaped mechanical resonator provides capacitive coupling between the feedline and microwave cavity. In addition, the device design allows application of both alternating current (ac) and direct current (dc) signals through the feedline.

The device is cooled down to 20 mK in a dilution refrigerator with sufficiently attenuated microwave input lines. Additional details of the low-temperature setup are included in the Supporting Information. The reflection from the cavity  $|S_{11}(\omega)|$  is measured using a vector network analyzer. Fig. 2(a) shows the measurement of  $|S_{11}(\omega)|$  with fundamental resonant mode at

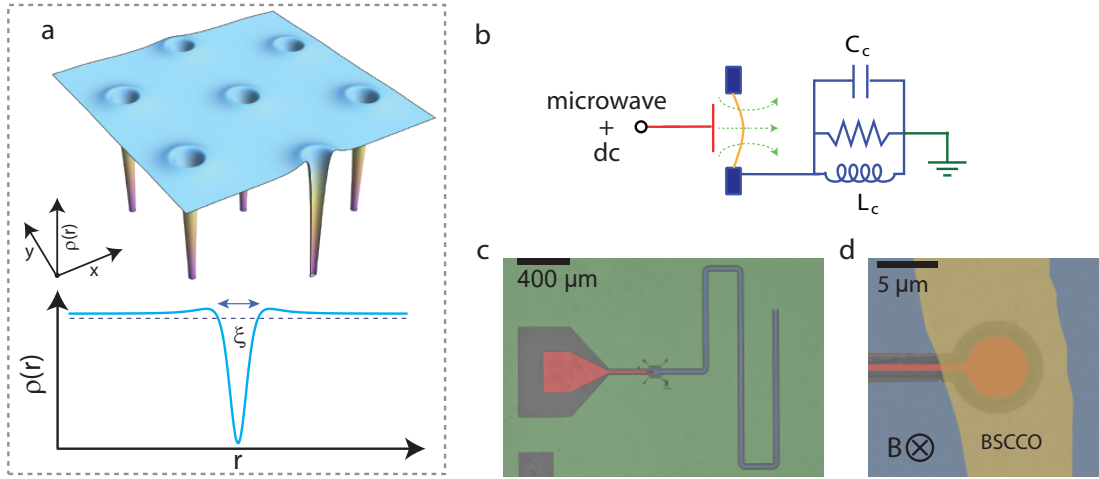


FIG. 1. **Cavity optomechanical architecture for detecting the vortex charge:** (a) Schematic showing the redistribution of the charge density at vortex core due to the chemical potential mismatch in the normal and in the superconducting state. The cyan curve shows the radial profile of the charge density redistribution around the vortex core and indicates the normal core of size of the coherence length  $\xi$ . (b) Electromechanical system with a single-port reflection cavity. The device is configured such that both direct current (dc) and microwave signals can be added to the drive port. The equivalent lumped inductance and capacitance are 1.42 nH and 350 fF, respectively. (c) Optical microscope image (false color) of the complete device. It shows a quarter-wavelength reflection-cavity in coplanar waveguide geometry patterned on an intrinsic Si substrate. (d) Scanning electron micrograph (false color) of the device near the coupling capacitor showing the suspended part of BSCCO flake which is 5 UC thick ( $\sim 15$  nm). The circular suspended part has a diameter of  $7 \mu\text{m}$ .

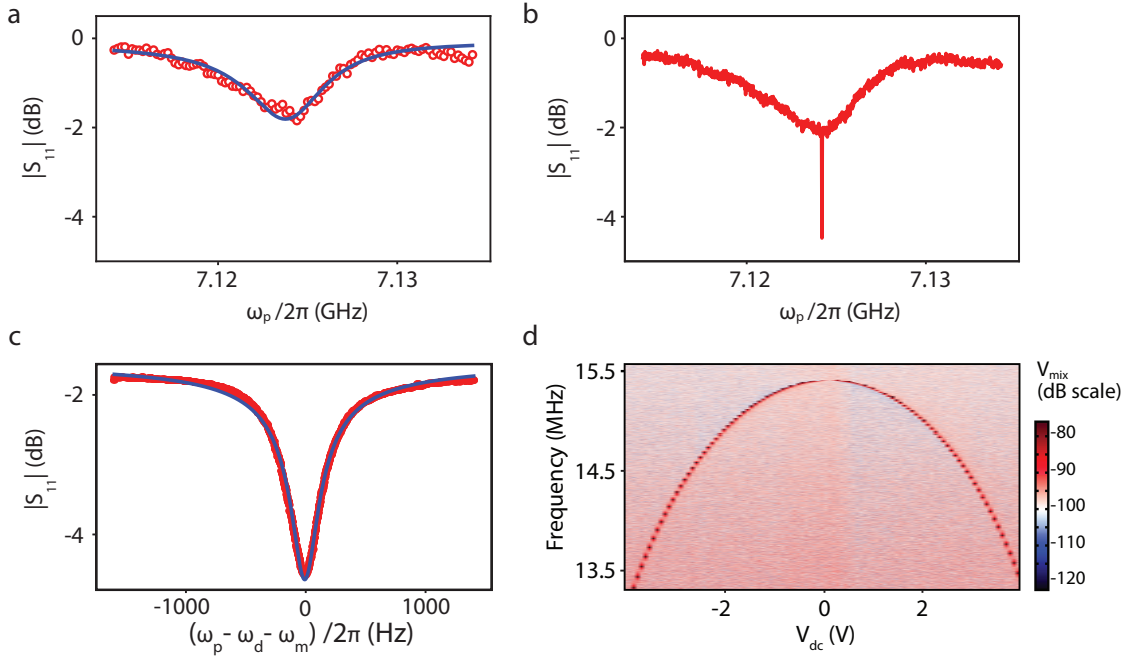


FIG. 2. **Optomechanically induced absorption (OMIA) measurements:** (a) Normalized reflection  $|S_{11}(\omega)|$  measurement of cavity at 20 mK. The blue line shows the fitted curve. (b) Measurement of  $|S_{11}(\omega)|$  in the presence of a red-detuned pump signal  $\omega_d = \omega_c - \omega_m$ . The sharp feature at the center of the cavity shows the optomechanically induced absorption (OMIA), resulting from the coherent oscillation of the mechanical resonator. (c) Zoomed-in view of the OMIA feature showing the detailed mechanical response. (d) Colorplot of the demodulated signal  $V_{mix}$  showing the quadratic tuning of the mechanical resonant frequency with  $V_{dc}$  applied at the feedline.

$\omega_c/2\pi = 7.124$  GHz. The solid line is the fit to the cavity response, yielding the internal and external linewidths of  $\kappa_i/2\pi = 0.48$  MHz and  $\kappa_e/2\pi = 4.92$  MHz, respectively.

For mechanical mode characterization, we drive the BSCCO resonator at its fundamental resonant frequency  $\omega_m$  using the radiation-pressure force. To achieve this, we add a pump signal at  $\omega_d = \omega_c - \omega_m$  along with a weak probe signal  $\omega_p$  near  $\omega_c$ . In the presence of the pump and the probe signals, the mechanical resonator experiences a beating radiation-pressure force near its resonant frequency which drives it coherently [17, 23, 24]. The mechanical motion of the resonator, in turn, modulates the intracavity pump field, resulting in an upconverted signal exactly at the probe frequency. As a coherent process, the upconverted signal interferes with the original probe signal and therefore results in an interference feature with linewidth set by the mechanical losses. Such interference in the cavity reflection is referred to as optomechanically induced absorption (OMIA) [17, 24].

The OMIA interference appears as a sharp absorption feature in the cavity response as shown in Fig. 2(b). A narrow span measurement of the absorption feature is shown in Fig. 2(c). The absorption dip directly manifests the coherently driven mechanical response, and thus allows the complete characterization of the mechanical resonator. From this measurement, we determine the fundamental mechanical mode frequency of  $\omega_m/2\pi \sim 15.383$  MHz and linewidth of  $\gamma_m/2\pi \sim 165$  Hz, corresponding to a quality factor of  $Q_m \sim 93000$ . The high quality factor is a direct indication of the low contact resistance between the MoRe film and BSCCO [22]. For the cavity-electromechanical device studied here, we estimated the single photon coupling rate  $g_0 = (\partial\omega_c/\partial x) x_{zp}$  to be  $2\pi \times 30$  Hz, where  $x_{zp}$  is the quantum zero-point motion of the BSCCO resonator.

Due to the novel electrical design of the device, we can add a dc voltage  $V_{dc}$  across the capacitor formed by the BSCCO resonator and the MoRe feedline underneath. While such a scheme has a significant advantage for probing the vortex charge [7], it allows characterization of the BSCCO resonator by an independent technique. A dc signal,  $V_{dc}$ , and an ac signal,  $V_{ac}$ , can be used to actuate the resonator by a force  $C_g V_{dc} V_{ac}/z_0$ , where  $z_0$  is the separation between BSCCO and the bottom electrode. By using the cavity as an interferometer, the mechanical mode is detected by demodulating the reflected microwave signal from the cavity. Fig. 2(d) shows the plot of demodulated signal ( $V_{mix}$ ) as  $V_{dc}$  is varied. We observe a quadratic tuning of the mechanical resonant frequency due to capacitive spring softening [25].

Having described the experimental technique, we measure the electromechanical response when a small magnetic field, perpendicular to the  $\text{CuO}_2$  plane of the BSCCO crystal is applied. It is represented in Fig. 1(d). We perform OMIA measurements while sweeping the magnetic field in the forward and reverse directions.

In the presence of the magnetic field, both the cavity frequency and the mechanical resonant frequency can change. Therefore, we first record the cavity response and readjust the pump frequency based on the measurement of  $\omega_c(B)$ . Fig. 3(a) shows the plot of the mechanical resonant frequency shift  $\Delta f_m(B) = f_m(B) - f_m(0)$  at  $V_{dc} = 0$  V. We limit the measurements in the range of  $\pm 32.6$  mT due to the reduction in the cavity quality factor at higher fields, which obscure the OMIA feature.

The hysteresis in  $\Delta f_m(B)$  suggests the role of flux-pinning, the Lorentz force of vortex transferring to the lattice and hence the irreversibility of the frequency shift, similar to the magnetostriction measurements on bulk single crystal of BSCCO [26]. For quantitative analysis, we use the critical state model, which is widely used to explain the magnetization of HTS [27, 28]. Here the maximum sheet current is capped at a critical current which in general could be magnetic field dependent [29, 30]. Due to this sheet current and the local magnetic field  $B_z(r)$ , the flake experiences a Lorentz force in the lateral direction. It results in a magnetic field dependent tension in the flake and hence a change in the mechanical resonant frequency as observed in Fig. 3(a).

We use a local critical sheet current as  $J_c(r) = J_{c0} \exp(-|B_z(r)|/B_0)$ , where  $B_z(r)$  is the local magnetic field in the BSCCO plane, and the maximum critical current  $J_{c0}$  and characteristic magnetic field  $B_0$  are two model parameters [29, 30]. We note that here BSCCO resonator thickness (5 UC) is much smaller than the London penetration length [31]. Therefore, a small field can push the flux-front, the boundary between the Meissner phase and the mixed phase, to nearly the center of the BSCCO flake. We assume that the steady-state critical currents remain confined to the boundaries of the BSCCO flake. To keep the calculations simple, we treat BSCCO as a thin circular plate. Calculation for the realistic geometry would only result in a scaling factor. Our model neglects geometrical [32] or Bean-Livingston barrier [33]. Furthermore, we assume no interaction between the vortex lines passing through the MoRe film (bottom capacitor plate) and BSCCO resonator (top capacitor plate).

To calculate the force experienced by the suspended part of the BSCCO flake, we first calculate the radial profile of the sheet current density  $J(r)$  and  $B_z(r)$  [34]. The Lorentz force on the suspended part of the BSCCO flake is then estimated by  $\int_0^R J(r) B_z(r) 2\pi r dr$ , resulting in a net stress in the flake. The stress can be compressive or tensile depending on the sign of the integral. The Lorentz-force induced stress can be used to compute the frequency shift of mechanical resonator, as shown by the solid lines in Fig. 3(a). The radial profiles of the local magnetic field and the normalized critical current are shown in Fig. 3(b). For these calculations, we have used the critical current density of  $J_{c0} = 3680$  A/ $\mu\text{m}$  [35, 36] and  $B_0 = 100$  mT [37]. Additional details of the model

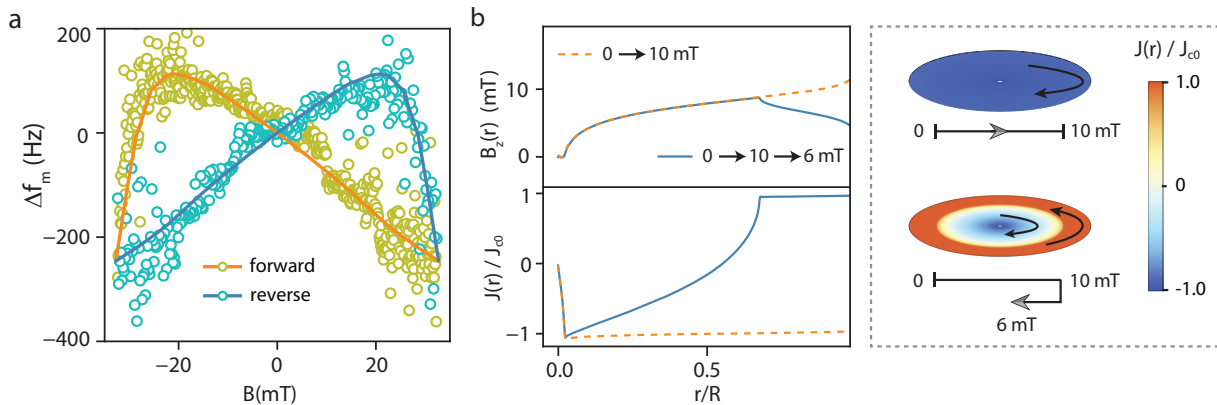


FIG. 3. **Modification of the mechanical response in the magnetic field:** (a) Shift in the mechanical frequency with magnetic field at  $V_{dc} = 0$  V, as magnetic field is swept in forward and reverse direction. The solid lines show the results obtained from the critical state model. (b) Plot of calculated local magnetic field and normalized critical current computed in the BSCCO plane. Dotted lines show the spatial profile after a forward sweep of  $B = 0$ -10 mT. Solid lines show the profiles for a subsequent field descent to  $B = 6$  mT. The side panel shows a side view of the normalized current distribution for the two cases stressing upon the change in the direction of current as field is lowered after reaching a maximum value.

are included in the Supporting Information..

To probe the charge associated with vortices, their interaction with the electrostatic field setup by a dc voltage plays a crucial role. Therefore, we now turn our focus on the mechanical response when  $V_{dc}$  is applied as shown schematically in Fig. 4(a). The plots of  $\Delta f_m$  at different  $V_{dc}$  applied across the BSCCO resonator are shown in Fig. 4(b-h). For these measurements, we sweep the magnetic field in  $\pm 16.3$  mT range due to the reduction in the mechanical quality factor at higher  $|V_{dc}|$ , which limits the measurement of mechanical response using OMIA technique. The measurement of  $\Delta f_m$  shows a clear asymmetry depending on the sign of  $V_{dc}$ . In addition, the overall dispersion with the magnetic field is enhanced at large negative dc voltages as compared to the case when  $V_{dc}$  is positive. The asymmetry in the electromechanical response with respect to the sign of  $V_{dc}$  (left vs right panels in Fig. 4(b-h) clearly suggests an electrostatic origin. This could be explained by considering the charge trapped in the vortex core. The charge per copper-oxide layer inside the vortex core is given by  $Q_c \sim |e|(\Delta/\epsilon_F)^2$  [4, 7]. Using  $\Delta/\epsilon_F \sim 0.1$ , and a  $\text{CuO}_2$ -plane spacing of 0.75 nm for BSCCO [38], a typical estimate of  $Q_c = 0.01 |e|$  can be made. It is equivalent to a line charge density  $Q_\xi$  of 0.013  $|e|/\text{nm}$ .

In the limit  $t \gg \xi$ , where  $t$  is the thickness of BSCCO, the net effect of the vortex line charge can effectively be captured by considering an equivalent surface electric dipole  $\vec{p}_0$  [7]. To understand our observations, we consider the interaction of surface dipoles  $\vec{p}_0$  with the electric field set up by  $V_{dc}$ . A dc voltage across the capacitor modifies the interaction energy by  $U_{dip}(z) = -\vec{p}_0 \cdot \vec{E}(z)$ , where  $\vec{E}$  is the electric field between the capacitor plates, and hence leads to an electromechanical coupling. As

magnetic field is increased, the number of vortices  $n_v(B)$  penetrating the suspended part of the BSCCO increases, as  $n_v(B) = (\pi R^2 |B|)/\Phi_0$ , where  $\Phi_0$  is the superconducting flux quantum and  $R$  is the radius of the suspended part of BSCCO. By considering a uniform distribution of the vortices on a triangular lattice across the BSCCO resonator, their contribution to the electromechanical energy can be calculated by summing over all the vortices present in the suspended part.

We include the electric dipole contribution along with the elastic, and the capacitive contribution to the total electromechanical energy  $U(z)$ . Therefore, the effective spring constant  $\partial^2 U(z)/\partial z^2$  and hence the mechanical resonant frequency can be determined. The solid lines in Fig. 4(b-h) show the calculated  $\Delta f_m(B)$  by including a dc voltage dependent energy in the electromechanical response. Here the curves are plotted taking a dipole magnitude of  $p_0 = 30 |e|a_B$  with a positively charged core, where  $a_B = 5.29 \times 10^{-11}$  m is the Bohr radius. It is important to point out here that the sign of the vortex core charge is determined by the oxygen doping level in the BSCCO crystal. For an overdoped (oxygen-rich) crystal, it is expected to be positive [39]. For a positively charged vortex core, the surface dipole moment points in an outward direction from the BSCCO surface regardless to the direction of the applied magnetic field. Therefore, the electromechanical response is expected show an asymmetry with respect to the electric field created by  $V_{dc}$ . For a positively charged vortex core, the mechanical resonant frequency is expected to show a softening (hardening) behavior for negative (positive)  $V_{dc}$  voltages as observed in the measurement. Details of the electromechanical spring constant calculation are provided in the Supporting Information. In next paragraph, we calculate

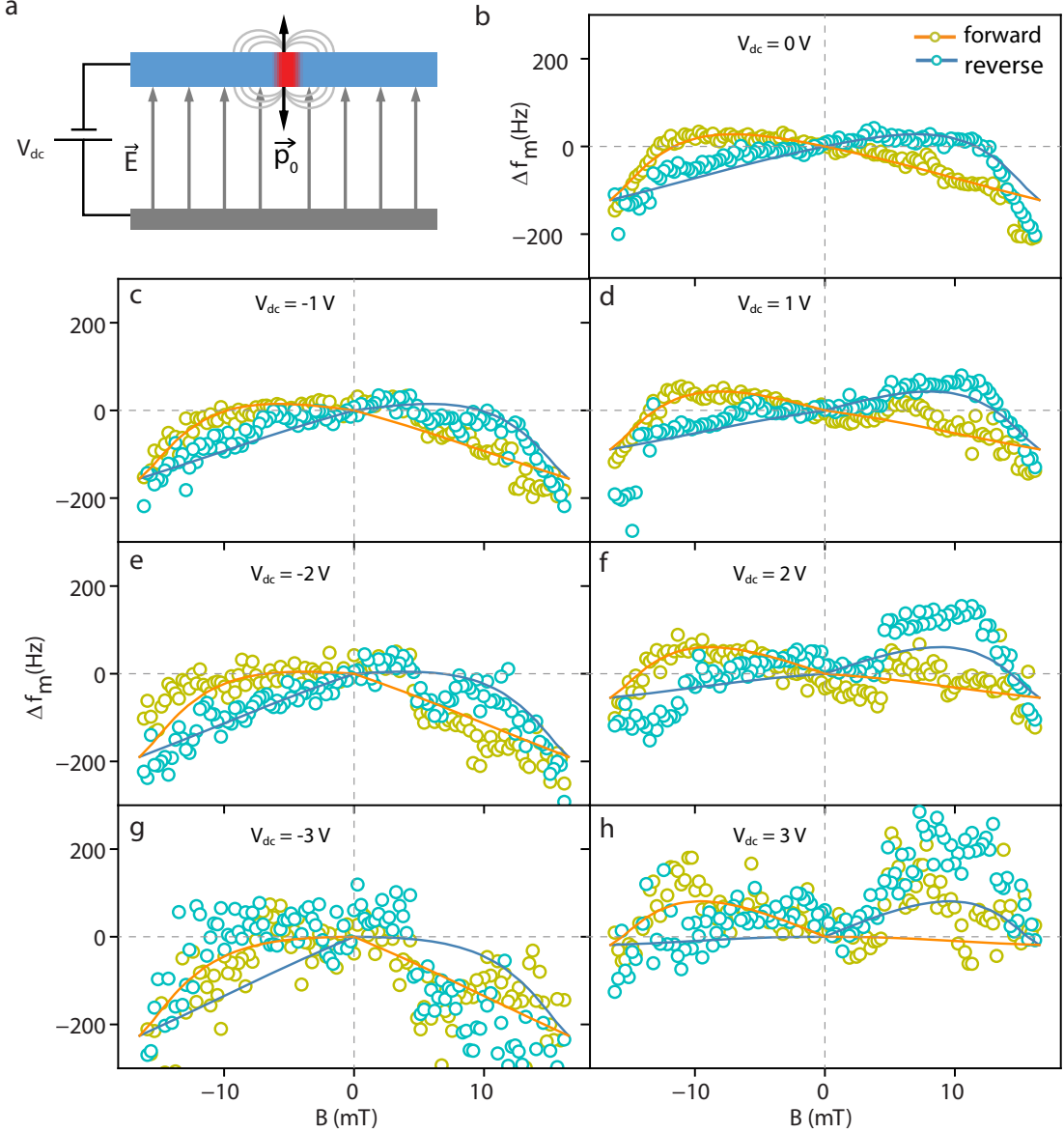


FIG. 4. **Evidence for the vortex-charge:** (a) A schematic showing the geometry of the capacitor formed by the BSCCO resonator (cyan) and MoRe plate (grey). The red part of BSCCO resonator represents a single vortex, showing two surface dipoles. (b-h) Measurement of shift in the mechanical frequency  $\Delta f_m = f_m(B, V_{dc}) - f_m(B = 0, V_{dc})$  as the magnetic field is swept in forward and reverse direction in the presence of a dc voltage  $V_{dc}$ . The solid lines are the calculated curves considering formation of the vortex-dipole.

the line charge density equivalent to this surface dipole moment and make a comparison with the values reported in the literature.

Following ref. [7], the charge density profile across a vortex core can be written as  $\rho(r) \sim (ea_B\zeta/\pi^3) (\xi^2 - r^2) / (\xi^2 + r^2)^3$ , where  $a_B$  is the Bohr radius, and  $\zeta$  is the particle-hole asymmetry parameter. The line charge density in the vortex core, therefore, is given by  $Q_\xi = \int_0^\xi \rho(r) 2\pi r dr = \zeta ea_B / (2\pi\xi)^2$ . Such a charge redistribution is equivalent to a surface dipole

pointing normal to the superconducting surface and having a magnitude of  $p_0 = (\zeta ea_B / \pi^2) (m/m_{eff}) \ln(z/\xi)$ . Therefore, the line charge can be related to the dipole moment as  $Q_\xi = p_0 (m_{eff}/m) (4\xi^2 \ln(z/\xi))^{-1}$ , where  $m_{eff}/m$  is the effective mass ratio of the charge carrier. Using  $\xi = 3.2$  nm [40],  $m_{eff}/m = 4.6$  [41], and  $z = 120$  nm, we obtain  $Q_\xi = +4.9 \times 10^{-2} |e|/\text{nm}$ , which is equivalent to a charge of  $+3.7 \times 10^{-2} |e|$  per  $\text{CuO}_2$  layer.

Our estimation of the charge per copper oxide layer is

consistent with the earlier measurements made on YBCO using the nuclear quadrupole resonance technique [9]. Both the experiments reveal a larger value of the vortex charge than that obtained via the theoretical predictions. The difference between the vortex charge magnitude from the experiments and the theory can have several interesting origins. First, it suggests that the gap anisotropy and Fermi surface curvature might be playing an important role [42]. Second, given the ultralow temperature in this experiment, the quantum effects in the vortex could become relevant. Finally, the nature of the vortex core could be different from the metallic phase [43, 44].

To summarize, we show clear evidence for the trapped charges in the vortex core probed using a cavity optomechanical device. The magnitude of the equivalent dipole is higher than the estimates from the BCS-theory while considering Thomas-Fermi screening. Such a difference opens up new possibilities to revisit the vortex-charge problem in atomically thin superconductors. Furthermore, our experiment and novel device approach show the advantages of integrating exfoliated thin flake into the cavity optomechanical devices for sensitive measurement of the thermodynamical properties. With minor modifications in the design, such technique could further be extended to other systems involving topological charge [45] or bosonic Landau levels [46]. This work thus opens up a new avenue to study quantum phase transitions as external parameters are varied.

### Acknowledgment

The authors thank Eli Zeldov, Subir Sachdev and Vijay Shenoy for insightful discussions. The authors also thank D. Jangade and A. Thamizhavel for their help during the crystal growth. M.M.D. acknowledges the Department of Atomic Energy of the Government of India under Grant No. 12-R&D-TFR-5.10-0100, DST Nanomission under Grant No. SR/NM/NS-45/2016 and SERB CORE grant CRG/2020/003836. V.S. acknowledges the research support under the Core Research Grant CRG/2018/001132 by DST and ISTC-0395 by STC-ISRO. S.K.S. acknowledges device fabrication facilities at the Department of Physics, and CeNSE, IISc-Bangalore funded by Department of Science and Technology (DST), Government of India.

---

\* v.singh@iisc.ac.in

- [1] Ketterson, J. B.; Song, S. N. *Superconductivity*; Cambridge University Press: Cambridge, 1999.
- [2] Abrikosov, A. A. Nobel Lecture: Type-II superconductors and the vortex lattice. *Reviews of Modern Physics* **2004**, *76*, 975–979.

- [3] Caroli, C.; De Gennes, P. G.; Matricon, J. Bound Fermion states on a vortex line in a type II superconductor. *Physics Letters* **1964**, *9*, 307–309.
- [4] Khomskii, D. I.; Freimuth, A. Charged Vortices in High Temperature Superconductors. *Physical Review Letters* **1995**, *75*, 1384–1386.
- [5] Feigel'man, M.; Geshkenbein, V.; Larkin, A.; Vinokur, V. M. Sign change of the flux-flow Hall effect in HTSC. *JETP Letters* **1995**, *62*, 834–840.
- [6] Koláček, J.; Lipavský, P.; Brandt, E. H. Charge Profile in Vortices. *Physical Review Letters* **2001**, *86*, 312–315.
- [7] Blatter, G.; Feigel'man, M.; Geshkenbein, V.; Larkin, A.; van Otterlo, A. Electrostatics of Vortices in Type-II Superconductors. *Physical Review Letters* **1996**, *77*, 566–569.
- [8] Hagen, S. J.; Lobb, C. J.; Greene, R. L.; Eddy, M. Flux-flow Hall effect in superconducting  $Tl_2Ba_2CaCu_2O_8$  films. *Physical Review B* **1991**, *43*, 6246–6248.
- [9] Kumagai, K.-i.; Nozaki, K.; Matsuda, Y. Charged vortices in high-temperature superconductors probed by NMR. *Physical Review B* **2001**, *63*, 144502.
- [10] Mitrović, V. F.; Sigmund, E. E.; Eschrig, M.; Bachman, H. N.; Halperin, W. P.; Reyes, A. P.; Kuhns, P.; Moulton, W. G. Spatially resolved electronic structure inside and outside the vortex cores of a high-temperature superconductor. *Nature* **2001**, *413*, 501–504.
- [11] Mounce, A. M.; Oh, S.; Mukhopadhyay, S.; Halperin, W. P.; Reyes, A. P.; Kuhns, P. L.; Fujita, K.; Ishikado, M.; Uchida, S. Charge-induced vortex lattice instability. *Nature Physics* **2011**, *7*, 125–128.
- [12] Bolle, C. A.; Aksyuk, V.; Pardo, F.; Gammel, P. L.; Zeldov, E.; Bucher, E.; Boie, R.; Bishop, D. J.; Nelson, D. R. Observation of mesoscopic vortex physics using micromechanical oscillators. *Nature* **1999**, *399*, 43–46.
- [13] Schwab, K.; Henriksen, E. A.; Worlock, J. M.; Roukes, M. L. Measurement of the quantum of thermal conductance. *Nature* **2000**, *404*, 974–977.
- [14] Chen, C.; Deshpande, V. V.; Koshino, M.; Lee, S.; Gondarenko, A.; MacDonald, A. H.; Kim, P.; Hone, J. Modulation of mechanical resonance by chemical potential oscillation in graphene. *Nature Physics* **2016**, *12*, 240–244.
- [15] Morell, N.; Tepsic, S.; Reserbat-Plantey, A.; Cepellotti, A.; Manca, M.; Epstein, I.; Isacson, A.; Marie, X.; Mauri, F.; Bachtold, A. Optomechanical Measurement of Thermal Transport in Two-Dimensional  $MoSe_2$  Lattices. *Nano Letters* **2019**, *19*, 3143–3150.
- [16] Šiškins, M.; Lee, M.; Mañas-Valero, S.; Coronado, E.; Blanter, Y. M.; van der Zant, H. S. J.; Steeneken, P. G. Magnetic and electronic phase transitions probed by nanomechanical resonators. *Nature Communications* **2020**, *11*, 2698.
- [17] Singh, V.; Bosman, S. J.; , B. H.; Blanter, Y. M.; Castellanos-Gomez, A.; Steele, G. A. Optomechanical coupling between a multilayer graphene mechanical resonator and a superconducting microwave cavity. *Nature Nanotechnology* **2014**, *9*, 820–824.
- [18] Weber, P.; Güttinger, J.; Tsioutsios, I.; Chang, D. E.; Bachtold, A. Coupling Graphene Mechanical Resonators to Superconducting Microwave Cavities. *Nano Letters* **2014**, *14*, 2854–2860.
- [19] Reserbat-Plantey, A.; Schädler, K. G.; Gaudreau, L.; Navickaite, G.; Güttinger, J.; Chang, D.; Toninelli, C.; Bachtold, A.; Koppens, F. H. L. Electromechanical con-

- trol of nitrogen-vacancy defect emission using graphene NEMS. *Nature Communications* **2016**, *7*, 10218.
- [20] Aspelmeyer, M.; Kippenberg, T. J.; Marquardt, F. Cavity optomechanics. *Reviews of Modern Physics* **2014**, *86*, 1391–1452.
- [21] Singh, V.; Schneider, B. H.; Bosman, S. J.; Merckx, E. P. J.; Steele, G. A. Molybdenum-rhenium alloy based high-Q superconducting microwave resonators. *Applied Physics Letters* **2014**, *105*, 222601.
- [22] Sahu, S. K.; Vaidya, J.; Schmidt, F.; Jangade, D.; Thamizhavel, A.; Steele, G.; Deshmukh, M. M.; Singh, V. Nanoelectromechanical resonators from high- $T_c$  superconducting crystals of  $\text{Bi}_2\text{Sr}_2\text{Ca}_1\text{Cu}_2\text{O}_{8+\delta}$ . *2D Materials* **2019**, *6*, 025027.
- [23] Weis, S.; Rivière, R.; Deléglise, S.; Gavartin, E.; Arcizet, O.; Schliesser, A.; Kippenberg, T. J. Optomechanically Induced Transparency. *Science* **2010**, *330*, 1520–1523.
- [24] Zhou, X.; Hocke, F.; Schliesser, A.; Marx, A.; Huebl, H.; Gross, R.; Kippenberg, T. J. Slowing, advancing and switching of microwave signals using circuit nanoelectromechanics. *Nature Physics* **2013**, *9*, 179–184.
- [25] Kozinsky, I.; Postma, H. W. C.; Bargatin, I.; Roukes, M. L. Tuning nonlinearity, dynamic range, and frequency of nanomechanical resonators. *Applied Physics Letters* **2006**, *88*, 253101.
- [26] Ikuta, H.; Hirota, N.; Nakayama, Y.; Kishio, K.; Kitazawa, K. Giant magnetostriction in  $\text{Bi}_2\text{Sr}_2\text{CaCu}_2\text{O}_8$  single crystal in the superconducting state and its mechanism. *Physical Review Letters* **1993**, *70*, 2166–2169.
- [27] Bean, C. P. Magnetization of Hard Superconductors. *Physical Review Letters* **1962**, *8*, 250–253.
- [28] Brandt, E. H. Superconductors of finite thickness in a perpendicular magnetic field: Strips and slabs. *Physical Review B* **1996**, *54*, 4246–4264.
- [29] Chen, D.; Goldfarb, R. B. Kim model for magnetization of type-II superconductors. *Journal of Applied Physics* **1989**, *66*, 2489–2500.
- [30] Senoussi, S.; Osséna, M.; Collin, G.; Campbell, I. A. Exponential  $H$  and  $T$  decay of the critical current density in  $\text{YBa}_2\text{Cu}_3\text{O}_{7-\delta}$  single crystals. *Physical Review B* **1988**, *37*, 9792–9795.
- [31] Harshman, D. R.; Kleiman, R. N.; Inui, M.; Espinosa, G. P.; Mitzi, D. B.; Kapitulnik, A.; Pfiz, T.; Williams, D. L. Magnetic penetration depth and flux dynamics in single-crystal  $\text{Bi}_2\text{Sr}_2\text{CaCu}_2\text{O}_{8+\delta}$ . *Physical Review Letters* **1991**, *67*, 3152–3155.
- [32] Zeldov, E.; Larkin, A. I.; Geshkenbein, V. B.; Konczykowski, M.; Majer, D.; Khaykovich, B.; Vinokur, V. M.; Shtrikman, H. Geometrical Barriers in High-Temperature Superconductors. *Physical Review Letters* **1994**, *73*, 1428–1431.
- [33] Bean, C. P.; Livingston, J. D. Surface Barrier in Type-II Superconductors. *Physical Review Letters* **1964**, *12*, 14–16.
- [34] Shantsev, D. V.; Galperin, Y. M.; Johansen, T. H. Thin superconducting disk with  $B$ -dependent  $J_c$ : Flux and current distributions. *Physical Review B* **1999**, *60*, 13112–13118.
- [35] You, L. X.; Yurgens, A.; Winkler, D. Superconducting critical current of a single  $\text{Cu}_2\text{O}_4$  plane in a  $\text{Bi}_2\text{Sr}_2\text{CaCu}_2\text{O}_{8+x}$  single crystal. *Physical Review B* **2005**, *71*, 224501.
- [36] Stangl, A.; Palau, A.; Deutscher, G.; Obradors, X.; Puig, T. Ultra-high critical current densities of superconducting  $\text{YBa}_2\text{Cu}_3\text{O}_{7-\delta}$  thin films in the overdoped state. *Scientific Reports* **2021**, *11*.
- [37] Sunwong, P.; Higgins, J. S.; Hampshire, D. P. Angular, Temperature, and Strain Dependencies of the Critical Current of DI-BSCCO Tapes in High Magnetic Fields. *IEEE Transactions on Applied Superconductivity* **2011**, *21*, 2840–2844.
- [38] Zhao, S. F.; Poccia, N.; Panetta, M. G.; Yu, C.; Johnson, J. W.; Yoo, H.; Zhong, R.; Gu, G.; Watanabe, K.; Taniguchi, T.; Postolova, S. V.; Vinokur, V. M.; Kim, P. Sign-Reversing Hall Effect in Atomically Thin High-Temperature  $\text{Bi}_{2.1}\text{Sr}_{1.9}\text{CaCu}_2\text{O}_{8+\delta}$  Superconductors. *Physical Review Letters* **2019**, *122*, 247001.
- [39] Chen, Y.; Wang, Z. D.; Zhu, J.-X.; Ting, C. S. Vortex Charges in High-Temperature Superconductors. *Physical Review Letters* **2002**, *89*, 217001.
- [40] Naughton, M. J.; Yu, R. C.; Davies, P. K.; Fischer, J. E.; Chamberlin, R. V.; Wang, Z. Z.; Jing, T. W.; Ong, N. P.; Chaikin, P. M. Orientational anisotropy of the upper critical field in single-crystal  $\text{YBa}_2\text{Cu}_3\text{O}_7$  and  $\text{Bi}_{2.1}\text{Sr}_{1.9}\text{CaCu}_2\text{O}_{8+x}$ . *Physical Review B* **1988**, *38*, 9280–9283.
- [41] Orlando, M. T. D.; Rouver, A. N.; Rocha, J. R.; Cavichini, A. S. Correlation among the effective mass ( $m^*$ ),  $\lambda_{ab}$  and  $T_c$  of superconducting cuprates in a Casimir energy scenario. *Physics Letters A* **2018**, *382*, 1486–1491.
- [42] Ueki, H.; Kohno, W.; Kita, T. Vortex-Core Charging Due to the Lorentz Force in a  $d$ -Wave Superconductor. *Journal of the Physical Society of Japan* **2016**, *85*, 064702.
- [43] Arovas, D. P.; Berlinsky, A. J.; Kallin, C.; Zhang, S.-C. Superconducting Vortex with Antiferromagnetic Core. *Physical Review Letters* **1997**, *79*, 2871–2874.
- [44] Knapp, D.; Kallin, C.; Ghosal, A.; Mansour, S. Antiferromagnetism and charged vortices in high- $T_c$  superconductors. *Physical Review B* **2005**, *71*, 064504.
- [45] Jiang, W.; Zhang, X.; Yu, G.; Zhang, W.; Wang, X.; Benjamin Jungfleisch, M.; Pearson, J. E.; Cheng, X.; Heimonen, O.; Wang, K. L.; Zhou, Y.; Hoffmann, A.; te Velthuis, S. G. E. Direct observation of the skyrmion Hall effect. *Nature Physics* **2017**, *13*, 162–169.
- [46] Devarakonda, A.; Suzuki, T.; Fang, S.; Zhu, J.; Graf, D.; Kriener, M.; Fu, L.; Kaxiras, E.; Checkelsky, J. G. Signatures of bosonic Landau levels in a finite-momentum superconductor. *Nature* **2021**, *599*, 51–56.

# Superconducting vortex-charge measurement using cavity electromechanics

Sudhir Kumar Sahu,<sup>1</sup> Supriya Mandal,<sup>2</sup> Sanat Ghosh,<sup>2</sup> Mandar M. Deshmukh,<sup>2</sup> and Vibhor Singh<sup>1,\*</sup>

<sup>1</sup>*Department of Physics, Indian Institute of Science, Bangalore-560012 (India)*

<sup>2</sup>*Department of condensed matter physics and material sciences, Tata Institute of Fundamental Research, Mumbai - 400005 (India)*

## I. MEASUREMENT SETUP

For microwave measurements, the device is mounted inside a microwave box and attached to the base plate of a dilution refrigerator at 20 mK. A coaxial cable is used as an input line with sufficient attenuators for microwave thermalization. The output signal is routed towards a HEMT amplifier using a coaxial line at 4 K stage followed by a microwave amplifier at room temperature. A cryogenic circulator is used to measure the reflection from the device. Between the circulator and the device port, we use a bias-tee and a low-pass filter, which allows us to add a dc voltage to the input feed-line of the cavity. A directional coupler is used to combine microwave tones in the input lines at room temperature. A detailed schematic of the measurement setup is given in Fig. S1(a).

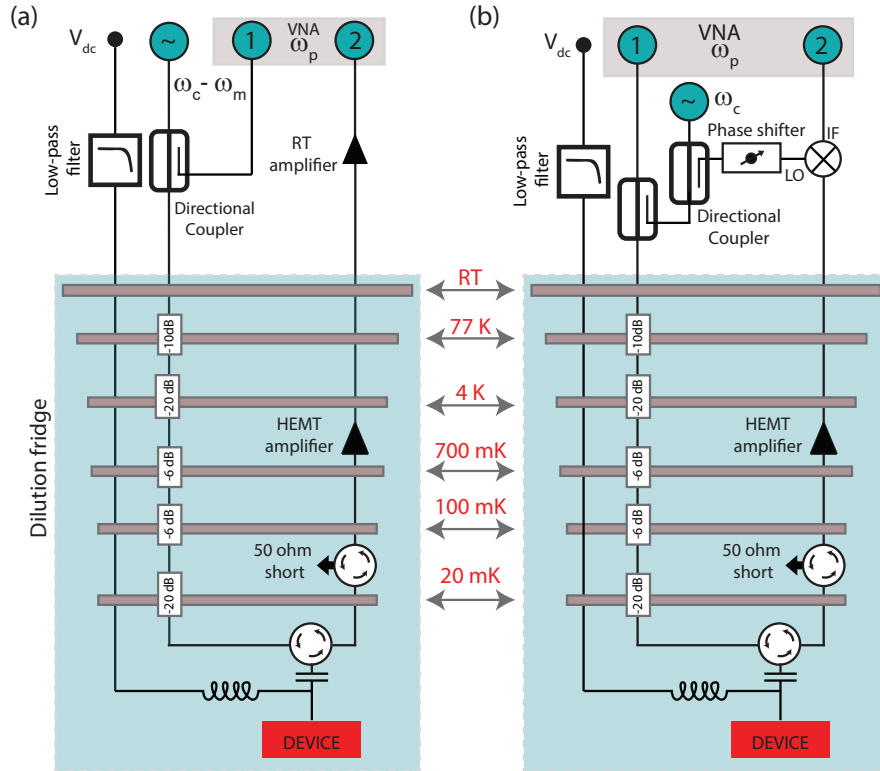


FIG. S1. (a) Schematic of the measurement setup for the OMIA measurements. (b) A schematic of the homodyne detection setup using a vector network analyzer (VNA). A mixer is used to demodulate the reflected signal from the cavity, and the intermediate frequency (IF) signal is sent to the receiving port of the VNA. For measurement setup inside the dilution refrigerator, we use Anritsu k250 bias tee, Pasternack PE8402 circulator and Raditek radc-4-8-Cryo-0.03-4K-S23-1WR-MS-b as isolator.

\* v.singh@iisc.ac.in



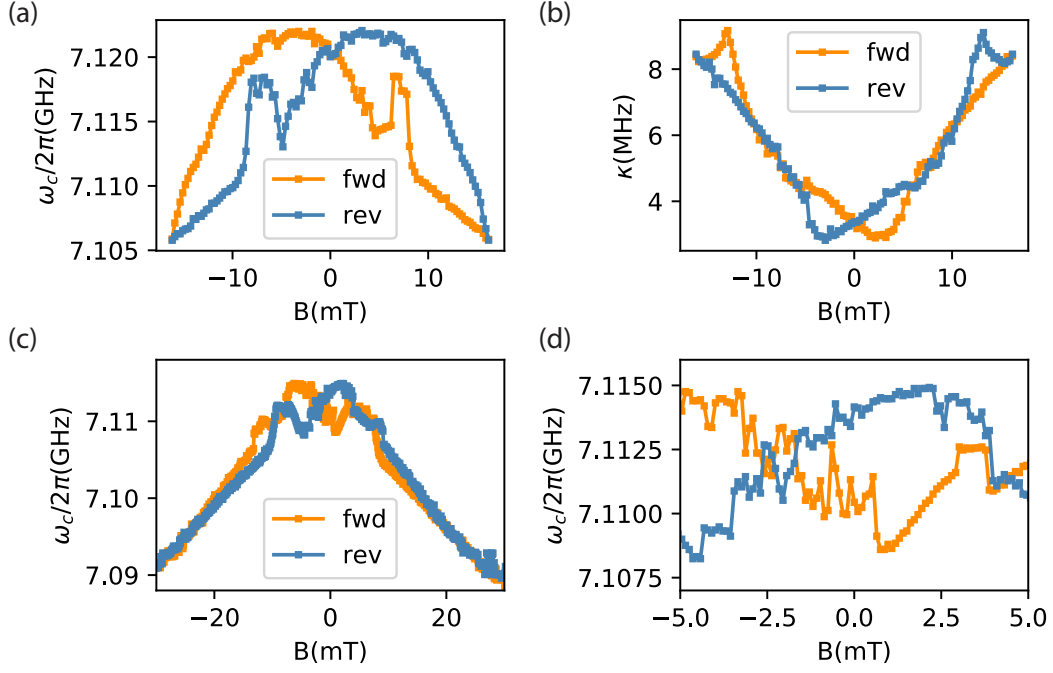


FIG. S2. (a, b) For the sample studied in the main text, the change in the resonant frequency and linewidth of the cavity, respectively. The magnetic field applied normal to the cavity plane is swept back-and-forth. An abrupt change in the cavity frequency indicates the movement of vortices in the film. (c, d) Change in the resonant frequency of the bare microwave cavity (a MoRe cavity without the BSCCO flake) as the magnetic field applied normal to the cavity plane is swept back-and-forth. The abrupt jumps are found in cavity resonant frequency.

### A. Cavity characterization

The microwave cavity is characterized by measuring the reflection coefficient  $|S_{11}(\omega)|$  using a vector network analyzer (VNA). While characterizing the microwave cavity, the pump power at  $\omega_c - \omega_m$  is kept off. To fit the reflection coefficient  $|S_{11}(\omega)|$ , we use

$$S_{11}(\omega) = \alpha e^{i\phi} + (1 - \alpha) \left( 1 - \frac{2\eta}{1 + \frac{2i(\omega - \omega_c)}{\kappa}} \right), \quad (\text{S.1})$$

where  $\alpha$  is the isolation of the circulator,  $\eta$  is the ratio between the external dissipation rate  $\kappa_e$  and the total dissipation rate  $\kappa$ ,  $\omega_c$  is the cavity resonant frequency and  $\phi$  is a phase arising from the propagation delay.

For the characterization of the microwave cavity in the magnetic field, the cavity resonant frequency and linewidth are measured with a step size of 0.25 mT as shown in Fig. S2(a) and Fig. S2(b) respectively. It is interesting to point out that the maximum cavity frequency and the minimum cavity linewidth occur at different applied magnetic fields. This is possibly due to the fact that the dominant contribution to the kinetic inductance and losses come from the different geometrical regions of the coplanar cavity [1]. While the kinetic inductance incorporates contributions from the vortices and the screening currents, the dissipation is dominated by the dynamics taking place near the current anti-node (short boundary condition of the resonator). Similar measurements of cavity resonant frequency were also carried out on a bare MoRe cavity as shown in Fig. S2(c). We observe similar jumps in cavity frequency, which signifies that such jumps are not unique to BSCCO based sample. Fig. S2(d) shows the zoomed-in view of the data set near the origin. The observation of jumps in the cavity frequency near zero magnetic field suggests the flux penetration at a field as small as 0.5 mT.

## B. Optomechanically-induced absorption measurements (OMIA)

For mechanical mode characterization in an OMIA setup, we use a pump tone at the red sideband ( $\omega_d = \omega_c - \omega_m$ ) and a probe tone ( $\omega_p$ ) near cavity frequency. Both the microwave tones are added using a directional coupler as shown in Fig. S1(a). As the magnetic field is swept, we first measure the cavity resonance as explained above at each set point. Subsequently, the red sideband pump tone and the cavity probe tone span are adjusted with the corresponding cavity frequency. The mechanical frequency is then calculated by fitting the OMIA response.

## C. Detection of mechanical mode using a low-frequency direct drive

The mechanical mode can also be characterized independently using a direct-drive method. A low-frequency RF signal  $V_{ac}$  and a dc signal  $V_{dc}$  are sent to the feedline to ‘electrostatically’ apply a force  $C'_g V_{ac} V_{dc}$  on the mechanical resonator, where  $C'_g$  is the derivative of flake capacitance with respect to displacement. Fig. S1 (b) shows the detailed circuit diagram for the homodyne measurement. In addition, a microwave tone at the resonant frequency of the cavity is added to the feedline. The motion of the mechanical resonator phase modulates the reflected signal from the cavity producing two sidebands at  $\omega_c \pm \omega_{ac}$ , where  $\omega_{ac}$  is the frequency of the  $ac$  drive. The reflected signal is then demodulated using an external mixer at room temperature. This way, the cavity is effectively used as an interferometer. The  $ac$  drive and the demodulated signals are controlled and recorded by a vector network analyzer; thereby a measurement of  $|S_{21}(\omega)|$  directly relates to the responsivity of the mechanical resonator. Fig. 2(d) of the main text shows the colorplot of demodulated signal where a sharp change in color indicates the mechanical resonance.

## II. ESTIMATION OF THE SINGLE-PHOTON COUPLING RATE

The measurement of OMIA feature allows us to characterize the optomechanical interaction in terms of cooperativity  $C = 4g^2/\kappa\gamma_m$ , where  $\kappa$  is the total cavity linewidth,  $\gamma_m$  is the mechanical linewidth,  $g = g_0\sqrt{n_d}$  is the linearized coupling strength and  $n_d$  is the number of pump photons in the cavity. At  $\omega_d = \omega_c - \omega_m$ , the reflection the cavity frequency is given by  $|S_{11}(\omega_c)| = \left| \frac{2\eta}{1+C} - 1 \right|$ . It thus allows to estimate cooperativity directly from the swing of the OMIA feature. Maximum cooperativity of 0.38 is achieved with 3 mW of red sideband pump power at the signal generator. Using the known attenuation in the setup,  $n_d$  was estimated using  $n_d = \frac{P_{in}\kappa_e}{\hbar\omega_d\left(\left(\frac{\kappa}{2}\right)^2 + (\omega_d - \omega_c)^2\right)}$ , where  $P_{in}$  is the power of the red sideband tone at the device input. Using the cooperativity results and the estimate of the number of photons, we expect the single photon coupling rate to be  $g_0/2\pi \approx 30$  Hz.

## III. ESTIMATION OF THE PRE-TENSION IN THE MECHANICAL MODE

The resonant frequency of the fundamental mode for a circular-shaped mechanical resonator clamped at the circumferences in the plate limit is given by [2]

$$f_p = \frac{10.21}{\pi} \sqrt{\frac{E}{3\rho(1-\nu^2)}} \left( \frac{t}{d^2} \right),$$

where  $t$  is the thickness,  $d$  is the diameter,  $E$  is the Young’s modulus of rigidity,  $\nu$  is the Poisson’s ratio and  $\rho$  is the volume mass density of the resonator. In the membrane limit, where pre-tension dominates over bending rigidity, the resonant frequency is given by [2]

$$f_t = \frac{2.4048}{\pi d} \sqrt{\frac{T}{\rho t}}.$$

In the cross-over limit, both the contribution from plate limit and membrane limit are comparable. Hence the resonant frequency can be approximated to  $f_m \approx \sqrt{f_p^2 + f_t^2}$  [3]. We measure the fundamental mode frequency of the BSCCO drum-head resonator to be 15.3826 MHz, a diameter of 7  $\mu\text{m}$  and a thickness of 15 nm (5 unit cells). Using  $E \sim 25$  GPa,  $\nu = 0.2$ , and the mass density  $\rho = 2360$  Kg/m<sup>3</sup>, we estimated the pre-tension  $T_0$  to be 0.732 N/m [4].

#### IV. ELECTROMECHANICAL RESPONSE IN THE MAGNETIC FIELD

To model the electromechanical response of the flake in the magnetic field, we consider the Lorentz force  $F_L = 2\pi \int_0^R J(r)B_z(r)rdr$  acting on the BSCCO flake in the radial direction, where  $J(r)$  is the screening current flowing in the circumferential direction and  $B_z(r)$  is the  $z$ -component of the local magnetic field. In the critical state, the Lorentz force is balanced by the pinning forces. Therefore, it leads to a magnetic field-dependent stress in the suspended flake. It can be obtained by  $T_L = \int_0^R J(r)B_z(r)dr$ . To obtain the profiles  $J(r)$  and  $B_z(r)$ , we use the exponential critical state model for thin flake and follow the treatment as prescribed by Shantsev *et al.* [5].

##### A. Critical State Model

The critical state models are widely used to explain the magnetic response of the high  $T_c$  superconductors. Here we consider a thin disk of radius  $R$  and thickness  $t$  such that  $\lambda^2/t \ll R$ , where  $\lambda$  is the London penetration depth. This disk is placed in a perpendicular magnetic field pointing in the  $z$ -direction. Here the maximum sheet current  $J_{c0}$  is defined as  $J_{c0} = j_{c0}t$ , where  $j_{c0}$  is the bulk critical current density at zero applied field. With this consideration, the self-consistent equations for the sheet current  $J(r)$ , local magnetic field  $B_z(r)$ , and applied magnetic field  $B$  can be written as

$$J(r) = \begin{cases} -\frac{2r}{\pi} \int_a^R \sqrt{\frac{a^2-r^2}{r'^2-a^2}} \frac{J_c[B_z(r')]}{r'^2-r^2} dr', & \text{if } r < a \\ -J_c[B_z(r)], & a < r < R \end{cases} \quad (\text{S.2})$$

$$B_z(r) = B + \frac{\mu_0}{2\pi} \int_0^R F(r, r') J(r') dr', \quad (\text{S.3})$$

$$B = B_c \int_a^R dr' \frac{1}{\sqrt{r'^2 - a^2}} \frac{J_c[B_z(r')]}{J_{c0}}, \quad (\text{S.4})$$

where  $a$  is the flux front position,  $B_c = \mu_0 J_{c0}/2$  and  $F(r, r') = K(u)/(r+r') - E(u)/(r-r')$ ,  $u(r, r') = 2\sqrt{rr'}/(r+r')$ , and  $K(u)$  and  $E(u)$  are the complete elliptic integrals of second kind defined as  $K(u) = \int_0^{\pi/2} [1 - u^2 \cos^2(x)]^{-1/2} dx$  and  $E(u) = \int_0^{\pi/2} [1 - u^2 \cos^2(x)]^{1/2} dx$ . For the exponential critical state model, we use  $J_c(B_z) = J_{c0} \exp(-|B_z|/B_0)$ .

After increasing the field to a maximum value of  $B_m$ , the field and current profiles for the subsequent descent are calculated as follows:

Let us denote the flux front position, the current density, and the field distribution at the maximum field as  $a_m$ ,  $J_m(r)$ , and  $B_{zm}(r)$ , respectively. During the magnetic field descent from  $B_m$ , the flux density becomes reduced in the outer region  $a < r < R$ , whereas the central part of the disk  $r < a$  remains frozen. During this process, local magnetic field  $B_z(r)$  and the sheet current  $J(r)$  given by

$$B_z(r) = B_{zm}(r) + \tilde{B}_z(r), \quad J(r) = J_m(r) + \tilde{J}(r). \quad (\text{S.5})$$

For the calculation of  $\tilde{B}_z(r)$  and  $\tilde{J}(r)$  similar procedure is used with a modification of  $J(r) = J_c[B_z(r)]$  in the region  $a < r < R$ . The complete set of equations for field descent are given by

$$\tilde{J}(r) = \begin{cases} \frac{2r}{\pi} \int_a^R \sqrt{\frac{a^2-r^2}{r'^2-a^2}} \frac{\tilde{J}_c[B_z(r')]}{r'^2-r^2} dr', & \text{if } r < a \\ \tilde{J}_c[B_z(r)], & a < r < R \end{cases} \quad (\text{S.6})$$

$$\tilde{B}_z(r) = B - B_m + \frac{\mu_0}{2\pi} \int_0^R F(r, r') \tilde{J}(r') dr', \quad (\text{S.7})$$

$$\frac{B - B_m}{B_c} = - \int_a^R dr \frac{1}{\sqrt{r^2 - a^2}} \frac{\tilde{J}_c[B_z(r)]}{J_{c0}}, \quad (\text{S.8})$$

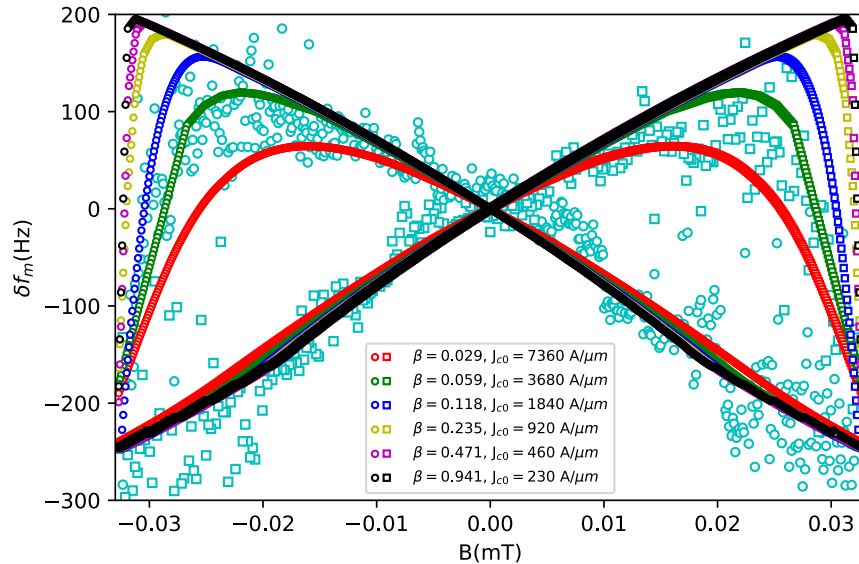


FIG. S3. Plot of the mechanical frequency shift with the magnetic field for different combinations of  $J_{c0}$  and  $\beta$ . Data with circle and square markers represent forward and reverse magnetic sweep, respectively.

where  $\tilde{J}_c(r) = J_c[B_{zm}(r) + \tilde{B}_z(r)] + J_c[B_{zm}(r)]$ .

The above equations are solved numerically using the following iterative method. First, a flux front position is defined, which decides the initial guess for the applied magnetic field  $B$ . Further,  $J_c$  is chosen to be independent of  $B(r)$  for initial guess with a value of  $J_{c0}$ . Equations are iterated with the initial guess until the solutions are converged. With  $B$  decreasing, the same procedure is used to find first  $J_m(r)$ ,  $B_{mr}(r)$ ,  $B_m$  for a given flux front position. Then, the equations for field descent are solved for a fixed flux front position yielding the functions  $\tilde{B}_z(r)$ ,  $\tilde{J}(r)$  and the applied field  $B$ . Then the value of  $B_z(r)$  and  $J(r)$  for field descent state is calculated using (S.5). Once  $B_z(r)$  and  $J(r)$  are obtained, the Lorentz force and the additional tension  $T_L$  in flake are calculated. The mode frequency of the BSCCO resonator is then given by

$$f_m(B) = \sqrt{\left(\frac{2.4048}{\pi d} \sqrt{\frac{T_0 + \beta T_L(B)}{\rho t}}\right)^2 + f_{plate}^2}, \quad (\text{S.9})$$

where  $\beta$  is a geometrical factor included to account for the non-uniform shape of the flake. We mention the possible origin of such a geometrical factor in the next paragraph. For  $\beta = 1/17 = 0.059$ , the measured and the calculated mechanical frequency shift with a perpendicular magnetic field are shown in Fig. 3(a) of the main text.

Due to the irregular shape of the entire BSCCO flake, the calculation of the screening current and the local magnetic field distribution is difficult. The critical state model discussed above assumes a circularly shaped BSCCO disk. Further, the non-uniform clamping of the suspended portion of the flake complicates the correction to the mechanical frequency shift due to the Lorentz force-induced stress. Therefore, the results obtained from the critical state model, assuming a circular geometry of the BSCCO flake, can not be directly applied. By introducing the geometrical parameter  $\beta$ , we try to capture these aspects in a phenomenological manner.

To show the deviations, we have plotted the mechanical frequency shift with the magnetic field using different combinations of  $J_{c0}$  and  $\beta$  in Fig. S3. Circular (square) data points represent the frequency shift for the forward (reverse) sweep of the magnetic field. For comparison, we have included the experimental data in cyan color. Variations in  $\beta$  and  $J_{c0}$  control the overall shape of hysteresis in the frequency shift. We find that the values of  $\beta = 0.059$  and  $J_{c0} = 3680 \text{ A}/\mu\text{m}$  produce results that resembles the experimental data. It is important to point out here that these choices do not modify the final estimate of the vortex charge.

## V. MODIFICATION OF THE ELECTROMECHANICAL RESPONSE WITH $V_{dc}$

To model the observed asymmetric change with respect to dc voltage, we include the energy of the effective surface dipoles formed by the flux-vortices [6]. When a dipole  $\vec{p}_0$  is placed in the electric field setup by the  $V_{dc}$ , it contributes  $-\vec{p}_0 \cdot \vec{E}(z)$  to the electromechanical energy. Assuming a uniform distribution of the vortices in the suspended portion of the BSCCO crystal, we can obtain their total contribution as

$$\begin{aligned} U_{dip}(z) &= -n_v(B) \times \vec{p}_0 \cdot \vec{E}(z) \\ &\approx n_v(B) \times p_0 \frac{V_{dc}}{z_0 + z}, \end{aligned} \quad (\text{S.10})$$

where  $n_v(B) = (\pi R^2 |B|) / \Phi_0$  is the total number of the vortices contained in the suspended portion of the flake,  $z_0 = 120$  nm is the equilibrium separation between the “plates” of the BSCCO capacitor with a capacitance  $C_g$ , and  $\Phi_0$  is the superconducting flux quantum. We emphasize here that it is precisely the linear dependence on  $V_{dc}$  that results in the asymmetry in the response with respect to the dc voltage.

With the dipole energy added, the total electromechanical energy of the drum can be written as,

$$\begin{aligned} U(z) &= U_{elastic} + U_{electrostatic} + U_{dip} \\ &= \frac{1}{2} k_m z^2 - \frac{1}{2} C_g(z) V_{dc}^2 + n_v(B) p_0 \frac{V_{dc}}{z_0 + z}, \end{aligned} \quad (\text{S.11})$$

where  $k_m = M \times (2\pi f_m(B, V_{dc} = 0))^2$  is the mechanical spring constant,  $M$  is the total mass of the resonator. With this total energy, the effective spring constant can be obtained as,

$$\begin{aligned} k_{eff}(B, V_{dc}) &= \frac{\partial^2 U(z)}{\partial z^2} \\ &= k_m - \frac{1}{2} \frac{\partial^2}{\partial z^2} C_g V_{dc}^2 + 2n_v(B) p_0 \frac{V_{dc}}{z_0^3}. \end{aligned} \quad (\text{S.12})$$

Results obtained from this equation are plotted in the Fig. 4 of the main text by defining,  $f_m(B, V_{dc}) = \frac{1}{2\pi} \sqrt{\frac{k_{eff}}{M}}$ .

## VI. OPTOMECHANICAL SPRING EFFECT

In a cavity optomechanical device, the measurement of mechanical resonant frequency can be affected due to the back action from the radiation-pressure force. The shift in the mechanical frequency while driving the system at red sideband is given by [7]

$$\delta f_m = g_0^2 \frac{P_{in}}{\hbar \omega_d} \frac{\kappa_e}{(\kappa^2/4) + \omega_m^2} \left( \frac{-2\omega_m}{(\kappa^2/4) + 4\omega_m^2} \right),$$

where  $P_{in}$  is the input drive power,  $g_0$  is the single photon coupling strength, and  $\kappa = \kappa_i + \kappa_e$  is the total dissipation rate of the microwave cavity. A constant shift in the mechanical frequency does not affect the results obtained in the magnetic field. However, due to the magnetic field dependent loss rate of the cavity, the circulating energy in the cavity ( $\hbar \omega_d n_d$ ) changes. It thus leads to a shift in the mechanical resonant frequency. As our device operates in the resolved-sideband limit ( $\kappa < \omega_m$ ), the correction to the mechanical frequency due to change in cavity linewidth is very small. Using estimated injected power of -61 dBm and a variation in  $\kappa$  from 4 MHz to 9 MHz, we calculated the worst-case shift in the mechanical frequency to be  $\sim 8$  Hz.

## VII. SCREENING OF THE MAGNETIC FIELD BY A SUPERCONDUCTING DISK

To understand the magnetic field screening by the MoRe electrode, positioned underneath the BSCCO flake, we take two approaches. First, we treat MoRe as a type-I superconductor having the London penetration length  $\lambda$ . We write down the governing equations for the vector potential as described by Caputo et al. [8]. Using the finite-element techniques, we numerically solve these equations to obtain the magnetic field at the position of the BSCCO flake (*i.e.*

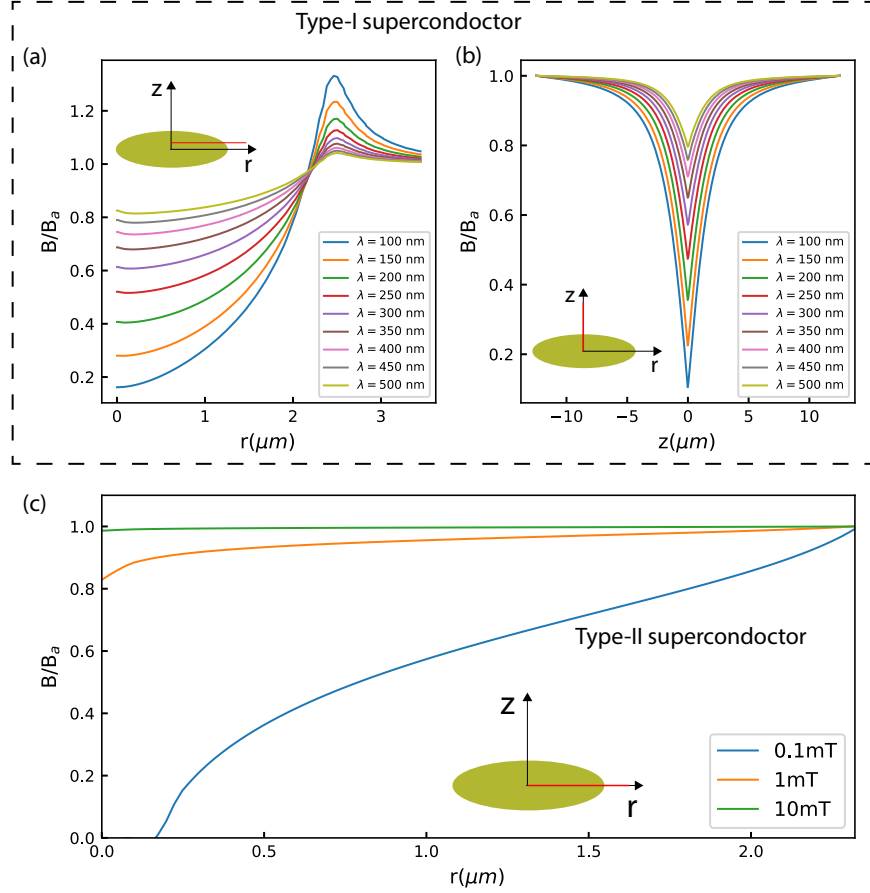


FIG. S4. Screening by a superconducting disk in an applied magnetic field  $B_a$  along the axis of the disk: Results obtained from FEM simulations assuming a type-I superconductor for different values of penetration length. (a) Plot of the normalized magnetic field the center of the disk along the radial direction in a plane 120 nm above the disk. The inset shows the schematic of the disk and its orientation. (b) Plot of the normalized magnetic field along the axis of the disk. (c) Results from the critical state model for a type-II superconductor: Normalized field at the surface of MoRe disk plotted from the center of the disk along the radial direction. The radius of the disk is taken as  $2.5 \mu\text{m}$ .

120 nm above the MoRe electrode). We consider a  $5 \mu\text{m}$  diameter and 80 nm thick circular superconducting disk placed in a magnetic field parallel to the axis of the disk. Fig. S4 (a) shows the plot of the normalized magnetic field strength at different radial distances in a plane 120 nm above the disk. In addition, Fig. S4 (b) shows the plot of the normalized magnetic field along the axis of the disk. We see that as the penetration length is increased, the magnetic field screening by the bottom disk deteriorates. For  $\lambda = 500 \text{ nm}$ , nearly 75 % of the magnetic field is recovered at the location of the BSCCO flake.

Since MoRe is a type-II superconductor, we use the critical state model to compute the normal component of the magnetic field at the surface of the bottom electrode. We use a critical current density of  $J_{c0} = 6.2 \times 10^8 \text{ A/m}^2 \times 80 \text{ nm}$  [9], and  $B_0 = 100 \text{ mT}$ . The calculated local magnetic field for 3 different values of applied magnetic field is plotted in Fig. S4 (c). These results suggest that the MoRe bottom electrode offers negligible screening for the perpendicular magnetic field.

TABLE I. Device parameter table

Parameter	Value
$g_0/2\pi$	30 Hz
$\omega_c/2\pi(V_{dc} = 0, B = 0)$	7.124 GHz
$\omega_m/2\pi(V_{dc} = 0, B = 0)$	15.383 MHz
typical probe photons	$0.15 \times 10^6$
typical drive photons	$0.55 \times 10^6$
total mass of resonator ( $M$ )	$1.3 \times 10^{-15}$ kg
quantum zero point motion ( $x_{zp}$ )	20 fm
BSCCO drum capacitance $c_g$	2.1 fF
coherence length of BSCCO ( $\xi$ )	3.2 nm
effective mass ratio of charge carrier $m_{eff}/m$	4.6

- 
- [1] Bothner, D.; Gaber, T.; Kemmler, M.; Koelle, D.; Kleiner, R.; Wünsch, S.; Siegel, M. Magnetic hysteresis effects in superconducting coplanar microwave resonators. *Physical Review B* **2012**, *86*, 014517.
- [2] Timoshenko, S. *Vibration Problems in Engineering*, 2nd ed.; Wolfenden Press: New York, 2007.
- [3] Castellanos-Gomez, A.; van Leeuwen, R.; Buscema, M.; van der Zant, H. S. J.; Steele, G. A.; Venstra, W. J. Single-Layer MoS<sub>2</sub> Mechanical Resonators. *Advanced Materials* **2013**, *25*, 6719–6723.
- [4] Sahu, S. K.; Jangade, D.; Thamizhavel, A.; Deshmukh, M. M.; Singh, V. Elastic properties of few unit cell thick superconducting crystals of Bi<sub>2</sub>Sr<sub>2</sub>CaCu<sub>2</sub>O<sub>8+ $\delta$</sub> . *Applied Physics Letters* **2019**, *115*, 143102.
- [5] Shantsev, D. V.; Galperin, Y. M.; Johansen, T. H. Thin superconducting disk with  $B$ -dependent  $J_c$ : Flux and current distributions. *Physical Review B* **1999**, *60*, 13112–13118.
- [6] Blatter, G.; Feigel'man, M.; Geshkenbein, V.; Larkin, A.; van Otterlo, A. Electrostatics of Vortices in Type-II Superconductors. *Physical Review Letters* **1996**, *77*, 566–569.
- [7] Aspelmeyer, M.; Kippenberg, T. J.; Marquardt, F. Cavity optomechanics. *Reviews of Modern Physics* **2014**, *86*, 1391–1452.
- [8] Caputo, J.-G.; Gozzelino, L.; Laviano, F.; Ghigo, G.; Gerbaldo, R.; Noudem, J.; Thimont, Y.; Bernstein, P. Screening magnetic fields by superconductors: A simple model. *Journal of Applied Physics* **2013**, *114*, 233913.
- [9] Sundar, S.; Sharath Chandra, L. S.; Sharma, V. K.; Chattopadhyay, M. K.; Roy, S. B. Electrical transport and magnetic properties of superconducting Mo<sub>52</sub>Re<sub>48</sub> alloy. *AIP Conf. Proc.* **2013**, 1092–1093.